**Derivation of depolarization ratios of aerosol fluorescence and water vapor Raman backscatters from lidar measurements**

Igor Veselovskii[1], Qiaoyun Hu[2], Philippe Goloub[2], Thierry Podvin[2], William Boissiere[2], Mikhail Korenskiy[1], Nikita Kasianik[1], Sergey Khaykyn[3], Robin Miri[2]

*[1]Prokhorov General Physics Institute of the Russian Academy of Sciences, Moscow, Russia.*

*[2]Univ. Lille, CNRS, UMR 8518 - LOA - Laboratoire d'Optique Atmosphérique, F-59650 Lille, France*

*[3]Laboratoire Atmosphère Observations Spatiales, UVSQ, CNRS, Sorbonne University, Guyancourt, France*

**Correspondence**: Qiaoyun Hu (qiaoyun.hu@univ-lille.fr)

**Abstract**

Polarization properties of the fluorescence induced by polarized laser radiation are widely considered in laboratory studies. In lidar observations, however, only the total backscattered power of fluorescence is analyzed. In this paper we present results obtained with a modified Mie-Raman-Fluorescence lidar operated at the ATOLL observatory, Laboratoire d'Optique Atmosphérique, University of Lille, France, allowing to measure depolarization ratios of fluorescence at 466 nm ($\delta_F$) and of water vapor Raman backscatter. Measurements were performed in May-June 2023 during the Alberta forest fires season when smoke plumes were almost continuously transported over the Atlantic Ocean towards Europe. During the same period, smoke plumes from the same sources were also detected and analyzed in Moscow, at the General Physics Institute (GPI), with a 5-channel fluorescence lidar able to measure fluorescence backscattering at 438, 472, 513, 560 and 614 nm. Results demonstrate that, inside the planetary boundary layer (PBL), the urban aerosol fluorescence is maximal at 438 nm, then it gradually decreases with increase of wavelength. The smoke layers observed within 4-6 km height present a maximum of fluorescence at 513 nm, while in the upper troposphere, fluorescence maximum shifts to 560 nm. Regarding the fluorescence depolarization ratio, for smoke its value typically varies within the 45-55 % range.

The depolarization ratio of the water vapor Raman backscattering at 408 nm is shown to be quite low (2±0.5%) in the absence of fluorescence, because the narrowband interference filter (0.3 nm) in the water vapor channel selects only the strongest vibrational lines of the Raman spectrum.

32 As a result, the depolarization ratio at the water vapor Raman channel is sensitive to the presence
33 of strongly depolarized fluorescence backscattering and can be used for evaluation of the aerosol
34 fluorescence contribution to measured water vapor mixing ratio.

36 **1. Introduction**

37      Possibility to measure the laser induced fluorescence becomes an important added-value to
38 existing Mie-Raman lidars, because fluorescence measurements provide new independent
39 information about aerosol properties. Nowadays, the spectroscopic lidars based on 32-channel
40 PMT combined with spectrograph proved the ability to measure the fluorescence spectrum
41 (Sugimoto et al., 2012; Reichardt, 2014; Reichardt et al., 2018, 2023, Richardson et al., 2019; Liu
42 et al., 2022). On the other hand, lidars, with a single fluorescence channel can be widespread due
43 to their simplicity (Rao et al., 2018; Veselovskii et al., 2020). Such single-channel fluorescence
44 lidar combined with depolarization measurements at the elastic wavelength, provide new
45 independent information about aerosol type (Veselovskii et al., 2022). However, in all lidar
46 studies, only the total scattered power was analyzed, while the polarization properties of the
47 fluorescence were ignored. At the same time, fluorescence depolarization measurements are
48 widely used in laboratory research (Lakowicz, 2006). When polarized laser radiation is used for
49 excitation, the fluorescence emission is also partly polarized and degree of its depolarization
50 (anisotropy) depends on the fluorescence lifetime, on the angle between excitation and emission
51 dipoles, and on the rotational mobility of molecules (Lakowicz, 2006). In the fluorescence
52 spectroscopy, the polarization state of emission is described by the anisotropy (Lakowicz, 2006),
53 introduced as:

54 $$r = \frac{P_F^{\square} - P_F^{\perp}}{P_F^{\square} + 2P_F^{\perp}} \tag{1}$$

55 where $P_F^{\square}$ and $P_F^{\perp}$ are the powers of co- and cross-polarized fluorescence components. In lidar
56 measurements, however, the fluorescence depolarization ratio, $\delta_F$ is given as.

57 $$\delta_F = \frac{P_F^{\perp}}{P_F^{\square}} \tag{2}$$

58 Therefore, the anisotropy is expressed as a function of the $\delta_F$ as follows:

59 $$r = \frac{1 - \delta_F}{1 + 2\delta_F} \tag{3}$$

For randomly oriented fluorophores with collinear absorption and emission dipoles, in the absence of rotational motion, the anisotropy r=0.4 (Lakowicz, 2006), which corresponds to $\delta_F$=33%. This is the minimal value one can expect in lidar measurements. Existence of any angle between absorption and emission dipoles, as well as molecule rotation in the process of emission will increase $\delta_F$ (Lakowicz, 2006). Thus, measurement of fluorescence depolarization ratio may bring additional information about atmospheric aerosol, as we will show below.

Water vapor is a key atmospheric component playing essential role in the planet's radiative balance, and Raman lidars today are widely used for such observations (Whiteman, 2003, Chouza et al., 2022 and references therein). However, when the UV laser beam passes through a smoke layer, the broadband fluorescence signal is induced and its spectrum includes the region of water vapor Raman lines. Thus, the signal in the water vapor channel (around 407.5 nm, when 354.7 nm lase radiation is emitted) becomes contaminated by the fluorescence backscatter signal (Immler et al.. 2005; Immler and Schrems, 2005). This contamination can be reduced by decreasing the width of the transmission band in the water vapor channel down to tenths of nm. However, as it was shown recently, fluorescence still remains the source of uncertainties, especially when the water vapor mixing ratio (WVMR) is measured inside the smoke layers in the upper troposphere (Chouza et al., 2022; Reichardt et al., 2023).

Depolarization measurements provide an opportunity to monitor the presence of fluorescence signal in the Raman channel. The Q-branch of water vapor Raman lines (near 407.5 nm) provides a weakly depolarized backscatter, while fluorescence is strongly depolarized. Thus, the presence of fluorescence should increase the depolarization ratio of signal in the water vapor channel. Moreover, if the depolarization ratios of water vapor and fluorescence are known, the contribution of fluorescence to the measured WVMR can be evaluated.

In this article, we report and analyze, for the first time, the depolarization ratio of aerosol fluorescence and of water vapor Raman backscatter from lidar observations performed at the ATOLL observatory (ATmospheric Observation at liLLe), Laboratoire d'Optique Atmosphérique, University of Lille, during dense smoke events occurred on May - June 2023. We start with a description of the experimental setup in Sect.2.1 and derive, in Sect. 2.2, the main equations for estimating the fluorescence contribution to the water vapor Raman channel. In the first part of the results section (Sect.3.1), the fluorescence depolarization ratios over ATOLL are analyzed for different aerosol types. The measurements of fluorescence spectra performed with a

91    new five-channel fluorescence lidar, operated in Moscow, are presented in Sect.3.2. In Sect. 3.3,

92    we analyze the depolarization ratio in the water vapor Raman channel and estimate the

93    contamination of fluorescence to the derived WVMR profiles. Finally, in Sect.4 we present our

94    conclusions.

95

96    **2. Experimental setup and data analysis**

97    *2.1 Lidar system*

98    In our study, two lidar systems are considered. The first one, LILAS ((LIlle Lidar

99    AtmosphereS) is a multiwavelength Mie-Raman-Fluorescence lidar, whereas the second one is a

100   multiwavelength fluorescence lidar operated by the General Physics Institute (GPI), Moscow

101   (Veselovskii et al., 2023). Both systems are based on a tripled Nd:YAG laser (Q-Smart 450) with a

102   20 Hz repetition rate and pulse energy about 100 mJ at 355 nm. The backscattered laser light in

103   both systems is collected by a 40 cm aperture telescope and the lidar signals are digitized with

104   transient recorders (Licel) with 7.5 m range resolution, allowing simultaneous detection in the

105   analog and photon counting mode.

106   LILAS allows the so called $3\beta+2\alpha+3\delta$ configuration, including three particle

107   backscattering ($\beta_{355}, \beta_{532}, \beta_{1064}$), two extinction ($\alpha_{355}, \alpha_{532}$) coefficients along with three particle

108   depolarization ratios ($\delta_{355}, \delta_{532}, \delta_{1064}$). The Raman channel with a 407.54/0.3 nm spectral width

109   interference filter allows also water vapor profiling. At the end of 2019, the lidar was modified to

110   enable fluorescence measurements. A part of the fluorescence spectrum is selected by a wideband

111   interference filter of 44 nm width centered at 466 nm (Veselovskii et al. 2020).

112   In the fluorescence lidar of GPI only 355 nm wavelength is emitted, while fluorescence is

113   measured in five spectral intervals. The central wavelengths and widths of spectral transmission

114   bands (in parentheses) are: 438(29), 472(32), 513(29), 560(40) and 614(54) nm (Veselovskii et al.,

115   2023). Thus, the fluorescence spectrum could be sampled at five different wavelengths. The

116   transmission bands of the fluorescence channels (Fig.1 in Veselovskii et al., 2023) are separated

117   and there are no cross-talks between the channels. At GPI, the measurements were performed at

118   an angle of 48 deg to the horizon. The strong sunlight background restricts the fluorescence

119   observations of both systems to only the nighttime hours.

120   Several aerosol properties can be derived from fluorescence. The fluorescence

121   backscattering coefficient, $\beta_{F\lambda}$, at wavelength $\lambda_F$ , is calculated from the ratio of fluorescence and

122  nitrogen Raman backscattering signals, as described in Veselovskii et al. (2020). We remind that

123  $\beta_{F\lambda}$ is related to fluorescence signals integrated over the filter transmission band $D_\lambda$. In Moscow

124  measurements are performed at five wavelengths, and to compare $\beta_{F\lambda}$ between different channels

125  one makes use of the "fluorescence spectral backscattering coefficient" $B_\lambda = \dfrac{\beta_{F\lambda}}{D_\lambda}$ (fluorescence

126  backscattering per spectral interval). LILAS has only one single fluorescence channel, therefore,

127  when presenting data from LILAS, for the sake of simplicity, one uses notation  $\beta_{F466}=\beta_F$. The

128  intensive property characterizing aerosol fluorescence is the fluorescence capacity $G_{F\lambda}$, which is

129  the ratio of the fluorescence backscattering at wavelength $\lambda_F$ to backscattering coefficient at laser

130  wavelength  $G_{F\lambda} = \dfrac{\beta_F}{\beta_\lambda}$. This ratio, in principle, can be calculated for any laser wavelength. For

131  LILAS observations $G_{F\lambda}$ is calculated with respect to $\beta_{532}$, as $\beta_{532}$ is derived with rotational Raman

132  scattering and it does not depend on assumption about the Angstrom exponent (Veselovskii et al.

133  2015). And again, when presenting LILAS data, for simplicity one will use the notation $G_{F\lambda}=G_F$.

134  In this work, all profiles of aerosol properties are smoothed with the Savitzky – Golay method,

135  using second order polynomials with 8 points in the spatial window.

136  Additional information about the atmospheric thermodynamic state was available from

137  radiosonde measurements performed at Herstmonceux (UK) and Beauvechain (Belgium) stations,

138  located 160 km and 80 km away from the ATOLL observatory, respectively. When calculating the

139  relative humidity, one then used the water vapor profiles measured by Raman lidar and temperature

140  profiles provided by the radiosonde.

141  As discussed in Sect.1, measurements of fluorescence depolarization ratio and

142  depolarization of water vapor Raman backscatter are expected to bring new information about

143  aerosol properties and fluorescence contamination in the water vapor Raman channel. In 2023,

144  LILAS was upgraded to allow depolarization measurements at both 466 nm and 408 nm. The

145  corresponding optical layout is shown in Fig.1. Dichroic mirrors DM separate the 387, 408 and

146  466 nm components, while polarizing cubes split the components with polarizations oriented

147  parallel (s) and perpendicular (p) to the emitted polarized laser beam. For both channels, the

148  polarizing cube PBS251 from ThorLabs was used. The fluorescence depolarization ratio, $\delta_F$ , and

149  the water vapor Raman scattering depolarisation ratio, $\delta w$ , are both defined and calculated as a

150  ratio of the perpendicular to the parallel respective components. The calibration of both ratios was

151 performed as described in Freudenthaler et al. (2009). The uncertainty of calibration is estimated

152 to be below 15% for both 466 and 408 nm channels.

153

154 **2.2 *Expressions for estimating fluorescence impact on water vapor measurements*.**

155 As discussed in the recent work of Chouza et al. (2022) and Reichardt et al. (2023), the

156 broadband aerosol fluorescence is expected to contribute to the signal measured at the water vapor

157 Raman channel. Below, we provide the basic equations for estimating this contribution, based on

158 the measurements of the depolarization ratio in the water vapor Raman channel. The elastic

159 backscattered radiative power, at the laser wavelength $\lambda_L$, from distance $z$, can be modeled, after

160 background subtraction, by writing the lidar equation:

$$161 \quad P_L = O(z)\frac{1}{z^2}C_L\beta T_L^2 \tag{4}$$

162 where $O(z)$ is the geometrical overlap factor, which is assumed to be the same for all channels. $C_L$

163 is a range independent constant, including efficiency of the detection channel, the emitted laser

164 power and the receiving telescope diameter. $T_L$ is the one-way atmospheric transmission,

165 describing light losses on the way from the lidar to distance $z$ at wavelength $\lambda_L$.

$$166 \quad T_L = \exp\left\{-\int_0^z [\alpha^a(\lambda_L, z') + \alpha^m(\lambda_L, z')]dz'\right\} \tag{5}$$

167 The backscattering and extinction coefficients contain the aerosol (*a*) and molecular (*m*)

168 contributions: $\beta_{\lambda_L} = \beta_{\lambda_L}^a + \beta_{\lambda_L}^m$ and $\alpha_{\lambda_L} = \alpha_{\lambda_L}^a + \alpha_{\lambda_L}^m$.

169 Radiative power in nitrogen Raman, water vapor Raman, and fluorescence channels can be

170 written in a similar way.

$$171 \quad P_R = O(z)\frac{1}{z^2}C_R\sigma_R N_R T_L T_R \tag{6}$$

$$172 \quad P_W = O(z)\frac{1}{z^2}C_W N_W \sigma_W T_W T_L \tag{7}$$

$$173 \quad P_F = O(z)\frac{1}{z^2}C_F\beta_F T_F T_L \tag{8}$$

174 where $C_R$, $C_W$, $C_F$ are the corresponding range independent constants. $T_R$, $T_V$, and $T_F$ are the one-

175 way transmissions at wavelengths $\lambda_R$, $\lambda_W$, $\lambda_F$, corresponding to the centers of transmission bands of

176 the channels. $N_R$ and $N_W$ are the concentrations in nitrogen and water vapor molecules while $\sigma_R$,

177     $\sigma_W$ are their Raman differential scattering cross sections respectively. The fluorescence

178     backscattering coefficient, $\beta_F$, is introduced the same way, as described in Veselovskii et al. (2020).

179         The received power of the fluorescence signal that leaks to the water vapor channel is:

180    
$$P_{FW} = O(z)\frac{1}{z^2}C_W\beta_{FW}T_W T_L \tag{9}$$

181     where $\beta_{FW}$ is fluorescence backscattering coefficient at wavelength $\lambda_W$. The WVMR, $n_W$, can be

182     obtained from Eqs. 6 and 7, if the calibration constant $K_W = \dfrac{C_R}{C_W}\dfrac{\sigma_R}{\sigma_W}$ is known:

183    
$$n_W = K_W\frac{P_W}{P_R}\frac{T_R}{T_W} \tag{10}$$

184         The fluorescence backscattering coefficient, $\beta_F$, derived from Eq.6 and Eq.8, also contains

185     the calibration constant $K_F$. The procedure of calibration is described in Veselovskii et al. (2020).

186     Finally, $\beta_F$ reads as:

187    
$$\beta_F = K_F n_R \frac{P_F}{P_R}\frac{T_R}{T_F} \tag{11}$$

188     where $n_R = \dfrac{N_R(z)}{N_R(z=0)}$ is the relative change of number density of nitrogen molecules with height.

189     The fluorescence signal $P_{FW}$ in the water vapor channel can be expressed from $P_F$ using parameter

190     $\eta$, which depends on the ratio of fluorescence cross sections at wavelengths $\lambda_W$ and $\lambda_F$, on the

191     filters width and on the efficiency of both channels, as follows:

192    
$$P_{FW} = P_F\eta\frac{T_W}{T_F} \tag{12}$$

193     The total signal measured in the water vapor channel, $\tilde{P}_W$, is the addition of both water vapor

194     backscatter, $P_W$, and the fluorescence backscatter, $P_{FW}$,

195    
$$\tilde{P}_W = P_W + P_{FW} = P_W + P_F\eta\frac{T_W}{T_F} \tag{13}$$

196     One should remember, that the fluorescence spectrum, even for the same type of aerosols, can vary

197     with altitude and from observation to observation, which finally influences $\eta$. To minimize this

198     influence it is desirable to keep $\lambda_W$ and $\lambda_F$ as close as possible.

199    If the received lidar signals at the water vapor Raman and fluorescence channels are
200    separated into co- polarized (*II*) and cross-polarized ($\perp$) components, in respect to the polarization
201    of the emitted laser beam, their powers at the water vapor Raman channel are `given` respectively:

202    $$\tilde{P}_W^{\square} = P_W^{\square} + P_F^{\square}\eta \frac{T_W}{T_F} \tag{14}$$

203    $$\tilde{P}_W^{\perp} = P_W^{\perp} + P_F^{\perp}\eta \frac{T_W}{T_F} = \delta_W P_W^{\square} + \delta_F P_F^{\square}\eta \frac{T_W}{T_F} \tag{15}$$

204    where $\delta_F$ and $\delta_W$ are the fluorescence and water vapor Raman depolarization ratios, defined as:

205    $$\delta_F = \frac{P_F^{\perp}}{P_F^{\square}} \quad \text{and} \quad \delta_W = \frac{P_W^{\perp}}{P_W^{\square}} \tag{16}$$

206    Here we assume that the depolarization ratio of fluorescence is the same at the wavelengths $\lambda_W$
207    and $\lambda_F$. This assumption is usually valid, because fluorescence emission is normally from the
208    lowest singlet state, so the depolarization ratio is spectrally independent (Lakowicz, 2006).

209    Due to the presence of fluorescence, the depolarization ratio measured at the water vapor
210    Raman channel is:

211    $$\tilde{\delta}_W = \frac{\tilde{P}_W^{\perp}}{\tilde{P}_W^{\square}} = \frac{\delta_W P_W^{\square} + \delta_F P_F^{\square}\eta \frac{T_W}{T_F}}{P_W^{\square} + P_F^{\square}\eta \frac{T_W}{T_F}} \tag{17}$$

212    Here $\delta_W$ is the depolarization ratio that would be measured at the water vapor Raman channel in
213    the absence of atmospheric fluorescence. From Eqs.9, 10, 14, 15, 17 the parameter $\eta$ can be derived
214    using the lidar measured values, such as the water vapor mixing ratio $\tilde{n}_W$, depolarization ratio $\tilde{\delta}_W$,
215    and fluorescence backscattering, $\beta_F$ :

216    $$\eta = \frac{\tilde{n}_W}{\beta_F} \frac{K_F}{K_W} n_R \frac{(1+\delta_F)(\tilde{\delta}_W - \delta_W)}{(1+\tilde{\delta}_W)(\delta_F - \delta_W)} \tag{18}$$

217    where $\tilde{n}_W$ is the WVMR containing the fluorescence contribution.

218    It should be noted, that the choice of calibration constants $K_F$, $K_W$ does not influence $\eta$, because
219    $\tilde{n}_W$ and $\beta_F$ are calculated using the same calibration constants. Finally, the increase of WVMR
220    $\Delta n_W$ induced by the fluorescence can be calculated as:

221 $$\Delta n_W = K_W \frac{P_F \eta \frac{T_W}{T_F}}{P_R} \frac{T_R}{T_W} = \frac{K_W}{K_F} \eta \beta_F \frac{1}{n_R} \qquad (19)$$

222     As soon as the parameter $\eta$ is calculated from Eq.18, we can estimate the relevant error

223 $\Delta n_W$ from $\beta_F$, which in the case of LILAS is measured at 466 nm (Veselovskii et al., 2020). In such

224 estimation we have to assume that the relationship between fluorescence at 466 nm and 408 nm

225 remains constant with height. A possibility to perform correction from single – channel

226 fluorescence measurements was discussed by Reichardt et al. (2023), where it was shown, that for

227 466/408 nm channels, correction actually may depend on height. The corresponding analysis based

228 on our measurements will be presented in Sect.3.2.

229     We should mention that when the depolarization at the water vapor Raman channel is

230 available, the contribution of fluorescence to WVMR can be obtained without using $\eta$. From

231 Eqs.18 and 19 we obtain:

232 $$\Delta n_W = \tilde{n}_W \frac{(1+\delta_F)\left(\tilde{\delta}_W - \delta_W\right)}{(1+\tilde{\delta}_W)\left(\delta_F - \delta_W\right)} \qquad (20)$$

233 However, such correction can be performed only at low altitudes, where the signal-to-noise ratio

234 at the cross-polarized water vapor channel is sufficient for calculation of $\tilde{\delta}_W$.

235

236     **3. Experimental results**

237     In May – June 2023, the Canadian forest fires were at the origin of numerous smoke layers

238 observations in a wide range of altitude, ranging from the PBL to the tropopause. The Boreal

239 wildfire season in 2023 started anomalously early. A wildfire in Alberta, Canada at 53.2° N, 115.7°

240 W has produced an intense Pyrocumulonimbus (PyroCb) cloud on 5 May with the minimum

241 satellite-derived infrared brightness temperature of -66° C, which should correspond to 10-11 km

242 altitude according to local radiosoundings. In order to describe the long-range transport of the

243 smoke plume produced by this event, we use UV absorbing Aerosol Index (AI) measurements by

244 the Ozone Monitoring and Profiling Suite (OMPS) Nadir Mapper (NM) instrument onboard Suomi

245 NPP satellite mission (Flynn et al., 2014). AI is widely used as a proxy of the amount of absorbing

246 aerosols (e.g smoke, dust, ash) and its dimensionless value is proportional to the altitude of the

247 aerosol layers. AI values above 15 are usually associated with smoke plumes at or above the

248   tropopause (Peterson et al., 2018 and references therein), whereas maximum AI value reported by
249   the OMPS-NM instrument for the Alberta event reached to 19.9.

250       Fig. 2 displays the spatio-temporal evolution of the smoke plume from the Alberta event
251   represented by the areas of enhanced AI observed between 5–21 May. The smoke in the upper
252   troposphere and lower stratosphere (UTLS) is advected by the westerly winds, crossing the
253   Atlantic about 1 week before reaching Moscow by 15 May. On that date, the Moscow lidar has
254   detected the smoke layer at 10-11 km (see Sect.3.2). The plume was then further advected across
255   Eurasia towards northeastern Siberia. By 22 May the smoke plume completes its first
256   circumnavigation (not shown) and passes over Lille on 23 May and then over Moscow for the
257   second time around 27 May. Thus, we can expect, that the smoke layers observed over Lille and
258   Moscow have the same source.

259

260       ### *3.1 Variability of fluorescence depolarization ratio*

261       At the first stage of our research we focused on the variability of the fluorescence
262   depolarization ratio for aerosol types. The main attention was paid to smoke particles, because
263   they provide the strongest impact on the Raman water vapor measurements due to their high
264   fluorescence capacity (Veselovskii et al., 2022).

265       Spatio-temporal distributions of the aerosol elastic and fluorescence backscattering
266   coefficients ($\beta_{532}$ and $\beta_F$), on the night 26-27 June 2023, are shown in Fig.3. Dense smoke layer
267   with $\beta_F$ as high as $7.0\times10^{-4}$ Mm$^{-1}$sr$^{-1}$ occurred within the 4.0-10.0 km height range. The HYSPLIT
268   back trajectories show that the air masses were transported from North America. The relative
269   humidity increased from 40% at 4 km to RH>90% at 7 km where formation of ice crystals started.
270   Vertical profiles of aerosol elastic and fluorescence backscattering coefficients ($\beta_{532}$ and $\beta_F$),
271   together with fluorescence capacity, are shown in Fig.3c. Inside the smoke layer, $G_F$ is about $3\times10^{-4}$
272   , which is a typical value for smoke (Veselovskii et al., 2022) whereas, above 6 km, it decreases
273   due to ice formation. The presence of ice crystals increased the particle depolarization ratio $\delta_{532}$
274   from 3% at 6 km to 20% at 8 km. Fluorescence signals are strongly depolarized. Inside the PBL,
275   $\delta_F$ was about 60% whereas above 2 km it dropped to approximately 45%. The processes of
276   hygroscopic growth and ice formation do not provide a noticeable impact on $\delta_F$ value. During May
277   – June observations, the depolarization ratio of smoke varied mainly inside the 45-55% range.

278        As discussed in our previous publications (Veselovskii, et al., 2022; Hu et al., 2022), the

279    fluorescence capacity of aged smoke varies inside the $(2.5\text{-}5.5)\times10^{-4}$ range, probably due to the

280    changes in smoke composition and conditions of atmospheric transport. However, during the

281    Alberta fires, several smoke plumes with high $G_F$ have been observed. The highest fluorescence

282    capacity was observed on the night 16-17 June 2023. Vertical profiles of the aerosol properties for

283    this episode are shown in Fig.4. Dense smoke layers with fluorescence backscattering exceeding

284    $10.0\times10^{-4}$ $Mm^{-1}sr^{-1}$ occurred within the 7.0 -9.0 km height range. In this case, the maximal value

285    of the fluorescence capacity reached $10.0\times10^{-4}$. Fluorescence depolarization ratio was measured

286    about 50% through the entire smoke layer and the process of ice formation (just like in Fig.3d)

287    does not influence $\delta_F$. Thus, in May - June 2023 strong variations of $G_F$ in the $(2.5\text{-}10.0)\times10^{-4}$

288    range were accompanied by relatively small variations of $\delta_F$ remaining in the 45-55% interval.

289        It is known that in the UTLS  smoke particles can reach depolarization ratio, $\delta_{532}$ , as high as

290    15-20% (Burton et al., 2015; Haarig et al., 2018; Hu et al., 2019; Baars et al., 2019; Ohneiser et

291    al., 2020). High values of the particle depolarization ratio are usually attributed to the complex

292    internal structure of smoke particles (Mishchenko et al., 2016). Two smoke events in the UTLS,

293    characterized by enhanced $\delta_{532}$, on 28-29 May and 3-4 June 2023, are illustrated on Fig.5. On 28-

294    29 May, three smoke layers, at ~ 3.5, 6.5 and 11.5 km can be distinguished. High depolarization

295    ratios, reaching 40% at altitudes of 9.8-10.5 km, are due to ice clouds. In the lower smoke plumes

296    ranging between 3.5 and 6.5 km, the particle depolarization did not exceed 8%, whereas above 11

297    km $\delta_{532}$ increased to 15%. High values of $\delta_{532}$ observed in the UTLS correlate with increase of $G_F$

298    and with fluorescence depolarization, $\delta_F$, up to $7.0\times10^{-4}$ and 70%, respectively. Similar behavior

299    was observed on 3-4 June, where depolarization ratio, $\delta_{532}$, above 11.5 km increased up to 15%,

300    simultaneously with an increase of $G_F$ and $\delta_F$ up to $9.5\times10^{-4}$ and 70% respectively. Thus, change

301    in particle morphology may affect the depolarization ratio at the fluorescence channel. Another

302    possibility is that, in the UTLS, not only the particle structure can change, but the composition as

303    well. At the current stage of analysis, we are not yet able to conclude about the mechanisms

304    explaining the increase of fluorescence depolarization in the UTLS.

305        Furthermore, we did not observe the effect of atmospheric humidity on smoke fluorescence

306    depolarization. However, inside the PBL the observed hygroscopic growth was accompanied by

307    an increase of $\delta_F$. During the 9-16 June 2023 period numerous particle hygroscopic growth cases

308    were observed in the PBL. One of such cases, on the night of 12-13 June, is shown in Fig.6. The

309  relative humidity increased inside the PBL from 50% to 70% causing an increase of $\beta_{532}$ near the

310  PBL top. Depolarization ratio $\delta_{532}$ decreased with height, since the particles in the process of

311  hygroscopic growth became more spherical. The fluorescence depolarization ratio, however,

312  increased inside the PBL from 50% to 70%.

313       All results obtained during 9-16 June, showing dependence of $\delta_F$ and $\delta_{532}$ on the relative

314  humidity, are summarized in Fig.7. Particle depolarization $\delta_{532}$ systematically decreased with RH

315  but, on 16 June, this dependence is not monotonic which could be due to the change of aerosol

316  composition with height.  At low RH (below 30%), the fluorescence depolarization ratio was about

317  50%. However, at RH about 90%, $\delta_F$ increased up to 70%. One of possible explanations for that

318  behavior could be an increase of rotational mobility of the molecules in the process of particle

319  water uptake.

320

321       ***3.2 Fluorescence spectrum sampled with a with 5-channel lidar***

322       The results presented in the previous section were obtained with a single channel

323  fluorescence lidar. However, for analyzing the variability of smoke properties (for example,

324  increase of the fluorescence capacity with height) it is important to have information about a wider

325  fluorescence spectrum. Moreover, to estimate the fluorescence contamination in the Raman water

326  vapor channel, a relationship between fluorescence backscattering at 466 nm and 408 nm is used.

327  Thus, we need to know the variability of the fluorescence spectrum in the short wavelength region.

328  In our recent work (Veselovskii et al., 2023) we presented the first results obtained with a 5-

329  channel fluorescence lidar in operation at the GPI. This lidar is able to measure the fluorescence

330  backscattering profiles at 5 spectral intervals centered at 438, 472, 513, 560, and 614 nm. During

331  May–June 2023, several smoke plumes originating from Alberta fires were transported over

332  Moscow. Although Lille and Moscow are very distant from each other (above 2200 km), smoke

333  plumes observed have the same origin, hence the fluorescence spectra measured over Moscow are

334  quite helpful for the analysis of the Lille data.

335       Fig.8 (a,b,c) present the fluorescence spectral backscattering coefficients, $B_\lambda$, for 3 smoke

336  events detected in the UTLS above 10, 8 and 10 km for 15, 31 May and 20 June 2023, respectively.

337  On 15 and 31 May smoke layers were also present inside the 4-6 km range. Inside the PBL the

338  strongest fluorescence was systematically detected at the 438 nm channel while, at higher altitudes,

339  the maxima shifted to 560 nm. As follows from Figs.8d-f, the ratio $B_{560}/B_{438}$ remained in the range

340  0.4 -0.7 inside the PBL, whereas this ratio increased above 2.0 in the UTLS. Thus, for smoke

341  events the maxima of the fluorescence spectrum shifted with height towards longer wavelengths.

342  The ratio $B_{513}/\beta_{355}$ also increased with height and, above 10 km, it reached the values of $1\times10^{-5}$

343  $nm^{-1}$. In the UTLS, the maximal fluorescence capacity, $G_F$, measured by LILAS at 466 nm (with

344  44 nm bandwidth filter) was about $10\times10^{-4}$. In the smoke layer, the ratio of backscattering

345  coefficients $\beta_{355}/\beta_{532}$ is about 2, so the maximal ratio $B_{466}/\beta_{355}$ derived from LILAS measurements

346  was about $1.1\times10^{-5}$ $nm^{-1}$. Thus, values obtained over Lille and over Moscow are in good

347  agreement.

348       The fluorescence spectra obtained for the above mentioned smoke plumes are shown in

349  Fig.9. The values of $B_\lambda$ are normalized to $B_{438}$. Inside the PBL, the maximum of fluorescence was

350  measured at 438 nm and it decreased with wavelength. In the smoke layers within 4-6 km, the

351  maximum of fluorescence is observed at 513 nm while, in the UTLS, the maximum shifted to 560

352  nm.

353       When applying Eq.19 to estimate the contribution of smoke fluorescence into the Raman

354  water vapor channel of  LILAS, we assumed that the ratio of the fluorescence backscattering at

355  466 nm to 408 nm ($B_{466}/B_{408}$), was constant. For the lidar in operation at GPI, the shortest available

356  wavelength was 438 nm, therefore, at least, one can estimate the variability of the ratio $B_{472}/B_{438}$.

357  Fig. 10 presents the vertical profiles of $B_{472}/B_{438}$ for 11 smoke events occurring during the 15 May-

358  20 June 2023 period. Inside the PBL, this ratio varied in the 0.6–1.0 range. The lowest values

359  correspond to urban aerosols while, values of $B_{472}/B_{438}$ close to 1.0, probably indicate the presence

360  of smoke particles inside the PBL. Smoke layers were observed mainly above 4.0 km and $B_{472}/B_{438}$

361  showed a tendency to increase in the UT. It is interesting that, for the period 15 May–1 June, the

362  ratio was close to 1.5 whereas after 1 June, it became close to 1.0,  which can be related to changing

363  of smoke source. Mean value of $B_{472}/B_{438}$ in the 4.0–11.0 km range over all observations is 1.38

364  with standard deviation of 0.23 (relative variation is about 17%). For the channels 466 nm and 408

365  nm the wavelength separation is larger, so one can expect a variation of $B_{466}/B_{408}$ in the smoke

366  layer to be above that value. It points out the difficulties to face when the estimation of the

367  fluorescence contamination to the Raman water vapor channel is performed from a single

368  fluorescence channel at 466 nm. This issue was also discussed by Reichardt et al. (2023).

369

370       *3.3 Estimation of fluorescence impact on water vapor Raman measurements*

371  Measuring the depolarization ratio at the water vapor Raman channel provides an

372  opportunity to control/evaluate the presence of fluorescence leak in this channel. These

373  depolarization measurements were performed over Lille during May – June 2023. Vertical profiles

374  of water vapor depolarization ratio $\tilde{\delta}_W$ together with $\tilde{n}_W$, $\beta_{532}$, $\beta_F$, and $G_F$ are shown in Fig.11 for

375  the night 8-9 June and 10-11 June 2023. On 8-9 June the aerosols were confined mainly below 5

376  km. The fluorescence capacity was about $1.0 \times 10^{-4}$ below 3.0 km, but above, $G_F$ increased up to

377  $2.5 \times 10^{-4}$, indicating to the presence of smoke particles. The depolarization ratio in the water vapor

378  channel was about 2% in the height range 1.5–3.5 km, where the values of $\tilde{\delta}_W$ ranging within 1.8-

379  2.0% were observed at this height range, where the contribution of fluorescence was insignificant.

380  The depolarization ratio $\delta_W$ was low, because the interference filter at the water vapor channel

381  selects only strongest Q-branch lines and most of rotational lines are blocked. The contribution of

382  fluorescence becomes noticeable above 3.5 km where $n_W$ dropped, resulting in an increase of $\tilde{\delta}_W$

383  up to ~3%. Below 1 km height we also observed an increase of $\tilde{\delta}_W$ up to 2.2%, where fluorescence

384  backscattering is enhanced. Similar values of $\tilde{\delta}_W$ were observed on 10-11 June, where the

385  depolarization ratio increased up to 2.5% inside the smoke layer observed at ~3.75 km and below

386  2.0 km.

387    As discussed in Sect. 2.2, the contribution of fluorescence to the WVMR channel can be

388  derived from Eq.20 if $\tilde{\delta}_W$ and $\delta_F$ are measured simultaneously. Fig.12 presents the modeling of

389  the relative error $\dfrac{\Delta n_W}{\tilde{n}_W}$, introduced by the fluorescence to the WVMR channel as a function of $\tilde{\delta}_W$.

390  The computations are performed for different fluorescence depolarization ratios $\delta_F$=50%, 60%,

391  70% to include both smoke and urban particles. A depolarization ratio in the Raman water vapor

392  channel in the absence of fluorescence was assumed to be $\delta_W$=2%. For a depolarization ratio $\tilde{\delta}_W$

393  below 3% the relative error $\dfrac{\Delta n_W}{\tilde{n}_W}$ did not exceed 3%. As follows from the fluorescence spectra in

394  Fig.9, the fluorescence of urban particles increases towards shorter wavelengths, thus one can

395  expect an impact of the urban aerosol fluorescence on the water vapor measurements. In practice,

396  however, we did not observe values of $\tilde{\delta}_W$ exceeding 3% in the PBL, thus, contribution of aerosol

397    in the PBL is not critical. The reason is due to the low fluorescence capacity (about one order lower

398    than that of smoke) and higher water vapor content, comparing to the free troposphere.

399    Vertical profiles of $\tilde{\delta}_W$ shown in Fig.11 become noisy at heights where $nw$ is low, and thus

400    $\tilde{\delta}_W$ cannot be used for correction of the fluorescence effect in the upper troposphere. To overcome

401    this, we derived the parameter $\eta$ from Eq.18 at low altitudes where $\tilde{\delta}_W$ values are available, and,

402    thus, these $\eta$ values can be used to calculate $\Delta nw$ from Eq.19 in the entire height range. In such an

403    approach, however, one has to assume that the relationship between fluorescence cross sections at

404    466 nm and 408 nm remains constant with height. As discussed in Sect. 3.2, such assumption can

405    yield significant bias in the calculation of $\Delta nw$, and, at this stage, we do not provide corrected

406    profiles of the WVMR.

407    For the accurate calculation of $\eta$ one needs smoke events with strongly enhanced $\tilde{\delta}_W$ values,

408    which are usually observed in the smoke layers with low WVMR. Such suitable events are shown

409    on the nights of 26-27 May and 5-6 June 2023 in Fig.13. On 26-27 May a smoke layer

410    characterized by high fluorescence ($\beta_F$ up to $5\times10^{-4}$ Mm$^{-1}$sr$^{-1}$) and low $\tilde{n}_W$ (below 0.2 g/kg) values

411    is observed at 3.5 km. The relevant fluorescence depolarization ratio was about 47% and $\tilde{\delta}_W$

412    increased from 2% up to 12% in the middle of this layer. The parameter $\eta$ calculated from Eq.18

413    inside this smoke layer was about $2\times10^{-3}$ (g/kg)/(Mm$^{-1}$sr$^{-1}$). On 5-6 June the depolarization ratio

414    $\tilde{\delta}_W$ in the smoke layer increased up to 10% and value of $\eta$ was very similar. The values of $\eta$ derived

415    for several smoke episodes varied in the range $(2\text{-}2.5)\times10^{-3}$ (g/kg)/(Mm$^{-1}$sr$^{-1}$). For the estimate of

416    $\Delta nw$ we used the mean value of $\eta=2.25\times10^{-3}$ (g/kg)/(Mm$^{-1}$sr$^{-1}$), which is suitable only for smoke,

417    while for particles in the PBL, $\eta$ can have a different value. However, in the PBL, the low

418    depolarization ratios of $\tilde{\delta}_W$ prevented us from calculating $\eta$.

419    Fig.14 presents the vertical profiles of WVMR, the fluorescence backscattering and the error

420    $\Delta nw$ introduced by the fluorescence in WVMR on 26-27 May, 28-29 May and 16-17 June. Smoke

421    layers with strong fluorescence occurred systematically in our upper tropospheric observations.

422    The current LILAS system is not powerful enough for deriving accurate water vapor measurements

423    above 10 km, however an increase of $\tilde{n}_W$ in the fluorescent smoke layers is visible. We remind that

424    Eq.19 for $\Delta nw$ contains the factor $\dfrac{1}{n_R}$ (inverse relative change of nitrogen number density), thus,

425    the fluorescence impact on WVMR will increase with height. The uncertainties $\dfrac{\Delta n_W}{\tilde{n}_W}$ for all events

426    considered are shown in Fig.14d. On 26-27 May and 28-29 May the uncertainty of $\dfrac{\Delta n_W}{\tilde{n}_W}$ at 11 km

427    is of the order of 100%. On 16 June the smoke layer is lower (at 9 km) and the uncertainty is about

428    50%. Our demonstration shows that smoke fluorescence can significantly impact the water vapor

429    measurements. The proposed approach, based on the analysis of the depolarization ratio of the

430    water vapor signal, has the potential for estimation and correction of this impact.

431    **4.  Conclusion**

432         This study is one of the first efforts to measure the depolarization ratio of fluorescence of

433    the atmospheric aerosols. Analysis of more than 30 spring and summer smoke events allows

434    evaluation of the main aerosol intensive properties, including fluorescence capacity, particle and

435    fluorescence depolarization ratio. The fluorescence capacity of smoke in the troposphere varied

436    within (2.5-10.0)$\times 10^{-4}$, however, in spite of strong $G_F$ variation, $\delta_F$ was remaining within a

437    relatively narrow interval 45-55%. Additional observations revealed that for smoke plumes in the

438    upper troposphere the fluorescence depolarization ratio increased up to 70%. At the moment, we

439    cannot fully explain the mechanism responsible for this $\delta_F$ increase. It can be related to complex

440    particle internal structure at high altitudes, as well as to the change of the chemical composition,

441    revealed by the shift of the maximum of the fluorescence spectra to longer wavelengths in the

442    upper troposphere (Fig. 9).

443         Inside the PBL, the fluorescence depolarization ratio was higher than that of smoke and

444    varied within the 50-70% range. Moreover, the fluorescence depolarization ratio of urban particles

445    strongly depends on the relative humidity and, in contrast to the elastic scattering, the

446    depolarization of fluorescence increases with RH. One possible origin of this phenomena could be

447    attributed to an increase of the rotational mobility of the molecules involved in the process of water

448    uptake.

449         The depolarization ratio of the Raman water vapor backscatter, in the absence of

450    fluorescence, appeared to be quite low ($\delta_W$=2±0.5%). As a result, the depolarization ratio of the

451    Raman water vapor backscatter is sensitive to the presence of strongly depolarized fluorescence

452 signals, and the contribution of fluorescence to the WVMR can be calculated from the measured

453 value $\tilde{\delta}_W$. However, with the lidar used in this work, measurements of $\tilde{\delta}_W$ are only possible up to

454 the middle troposphere, while the problem of the fluorescence interference is the most crucial in

455 UTLS. To estimate the impact of fluorescence on the WVMR in UTLS, the height independent

456 parameter $\eta$, linking fluorescence at 466 nm and at 408 nm, was used. Such an approach relies on

457 the assumption that $\eta$ remains constant and allows only a rough estimation of the correction term

458 for the WVMR, $\varDelta nw$.  One possible solution to increase the accuracy of $\varDelta nw$ is to implement an

459 additional shorter wavelength channel (438 nm or even shorter). Another technical solution could

460 be considered as the depolarization ratio of Raman water vapor backscatter is low, therefore the

461 408 nm channel can be efficiently equipped with a polarizing cube. Thus, the depolarized channel

462 at 408 nm can be used for fluorescence measurements. As the polarizing cubes work in a wide

463 spectral range, so one can select the region outside of the water vapor spectrum (400–418 nm) for

464 fluorescence monitoring. We plan this experiment as well as other innovative approaches with our

465 future high-power fluorescence lidar, LIFE (Laser Induced Fluorescence Explorer), whose start of

466 operation is scheduled for the beginning of 2024.

467

468 *Data availability*. Lidar measurements are available upon request
469 (philippe.goloub@univ-lille.fr).

470

471 *Author contributions*. IV processed the data and wrote the paper. QH and TP performed the
472 measurements in Lille. PG supervised the project and helped with paper preparation. WB modified
473 LILAS for polarization measurements. MK and NK performed the measurements in Moscow. SK
474 analyzed transport of smoke layers and RM derived RH profiles from lidar measurements.
475 .

476 *Competing interests*. The authors declare that they have no conflict of interests.

477

## Acknowledgement

479 We acknowledge funding from the CaPPA project funded by the ANR through the PIA under

480 contract ANR-11-LABX-0005-01, the "Hauts de France" Regional Council (project ECRIN) and

481 the European Regional Development Fund (FEDER). ESA/QA4EO program is greatly

482 acknowledged for supporting the observation activity at LOA.  The work from Q. Hu was

483 supported by Agence *Nationale* de Recherhce ANR (*ANR-21-ESRE-0013) through the*

484 OBS4CLIM project. Development of fluorescence lidar in Moscow was supported by Russian

485   Science Foundation (project 21-17-00114). The work of S. Khaykin was partly supported by the

486   Agence Nationale de la Recherche (ANR) 21-CE01- 335 0007-01 PyroStrat project.

487

**References**

489

490 Baars, H., Ansmann, A., Ohneiser, K., Haarig, M., Engelmann, R., Althausen, D., Hanssen, I.,
491     Gausa, M., Pietruczuk, A., Szkop, A., Stachlewska, I. S., Wang, D., Reichardt, J., Skupin, A.,
492     Mattis, I., Trickl, T., Vogelmann, H., Navas-Guzmán, F., Haefele, A., Acheson, K., Ruth, A.
493     A., Tatarov, B., Müller, D., Hu, Q., Podvin, T., Goloub, P., Veselovskii, I., Pietras, C.,
494     Haeffelin, M., Fréville, P., Sicard, M., Comerón, A., Fernández García, A. J., Molero
495     Menéndez, F., Córdoba-Jabonero, C., Guerrero-Rascado, J. L., Alados-Arboledas, L., Bortoli,
496     D., Costa, M. J., Dionisi, D., Liberti, G. L., Wang, X., Sannino, A., Papagiannopoulos, N.,
497     Boselli, A., Mona, L., D'Amico, G., Romano, S., Perrone, M. R., Belegante, L., Nicolae, D.,
498     Grigorov, I., Gialitaki, A., Amiridis, V., Soupiona, O., Papayannis, A., Mamouri, R.-E.,
499     Nisantzi, A., Heese, B., Hofer, J., Schechner, Y. Y., Wandinger, U., and Pappalardo, G.: The
500     unprecedented 2017–2018 stratospheric smoke event: decay phase and aerosol properties
501     observed with the EARLINET, Atmos. Chem. Phys., 19, 15183–15198,
502     https://doi.org/10.5194/acp-19-15183-2019, 2019.

503 Burton, S.P., Hair, J.W., Kahnert, M., Ferrare, R.A., Hostetler, C.A., Cook, A.L., Harper, D.B.,
504     Berkoff, T.A., Seaman, S.T., Collins, J.E., Fenn, M.A., and Rogers, R.R.: Observations of the
505     spectral dependence of linear particle depolarization ratio of aerosols using NASA Langley
506     airborne High Spectral Resolution Lidar, Atmos. Chem. Phys., 15, 13453–13473,
507     https://doi.org/10.5194/acp-15-13453-2015, 2015.

508 Chouza, F., Leblanc, T., Brewer, M., Wang, P., Martucci, G., Haefele, A., Vérèmes, H., Duflot,
509     V., Payen, G., and Keckhut, P.: The impact of aerosol fluorescence on long-term water vapor
510     monitoring by Raman lidar and evaluation of a potential correction method, Atmos. Meas.
511     Tech., 15, 4241–4256, https://doi.org/10.5194/amt-15-4241-2022, 2022.

512 Flynn, L., Long, C., Wu, X., Evans, R., Beck, C. T., Petropavlovskikh, I., McConville, G.,
513     Yu, W., Zhang, Z., Niu, J., Beach, E., Hao, Y., Pan, C., Sen, B., Novicki, M., Zhou, S., Seftor,
514     C.: Performance of the Ozone Mapping and Profiler Suite (OMPS) products, J. Geophys. Res.
515     Atmos., 119, 6181–6195, 2014. doi:10.1002/2013JD020467

516 Freudenthaler,V., Esselborn, M.,Wiegner, M.,Heese, B., Tesche, M. and co-authors:
517     Depolarization ratio profiling at severalwavelengths in pure Saharan dust during SAMUM
518     2006, *Tellus* 61B, 165–179, 2009.

519 Haarig, M., Ansmann, A., Baars, H., Jimenez, C., Veselovskii, I., Engelmann, R., and Althausen,
520     D.: Depolarization and lidar ratios at 355, 532, and 1064 nm and microphysical properties of
521     aged tropospheric and stratospheric Canadian wildfire smoke, Atmos. Chem. Phys., 18, 11847-
522     11861, https://doi.org/10.5194/acp-18-11847-2018, 2018.

523 Hu, Q., Goloub, P., Veselovskii, I., Bravo-Aranda, J.-A., Popovici, I. E., Podvin, T., Haeffelin,
524     M., Lopatin, A., Dubovik, O., Pietras, C., Huang, X., Torres, B., and Chen, C.: Long-range-
525     transported Canadian smoke plumes in the lower stratosphere over northern France, Atmos.
526     Chem. Phys., 19, 1173-1193, 2019. https://doi.org/10.5194/acp-19-1173-2019.

527 Hu, Q., Goloub, P., Veselovskii, I., and Podvin, T.: The characterization of long-range transported
528     North American biomass burning plumes: what can a multi-wavelength Mie-Raman-
529     polarization-fluorescence lidar provide? Atmos. Chem. Phys. 22, 5399–5414, 2022
530     https://doi.org/10.5194/acp-22-5399-2022

531 Immler, F. and Schrems, O.: Is fluorescence of biogenic aerosols an issue for Raman lidar
532     measurements? Proc. SPIE 5984, Lidar Technologies, Techniques, and Measurements for
533     Atmospheric Remote Sensing, 59840H, https://doi.org/10.1117/12.628959, 2005.

534 Immler, F., Engelbart, D., and Schrems, O.: Fluorescence from atmospheric aerosol detected by a
535     lidar indicates biogenic particles in the lowermost stratosphere, Atmos. Chem. Phys., 5, 345–
536     355, https://doi.org/10.5194/acp-5-345-2005, 2005.

537  Lakowicz, J. R.: Principles of Fluorescence Spectroscopy, Springer New York, NY, 2006.
538     https://doi.org/10.1007/978-0-387-46312-4

539 Liu, F., Yi, F., He, Y., Yin, Z., Zhang, Y., and Yu, C.: Spectrally Resolved Raman Lidar to
540     Measure Backscatter Spectra of Atmospheric Three-Phase Water and Fluorescent Aerosols
541     Simultaneously: Instrument, Methodology, and Preliminary Results, IEEE Transactions on
542     Geoscience and Remote Sensing, 60, 5703013, 2022, doi: 10.1109/TGRS.2022.3166191

543 Mishchenko MI, Dlugach JM, Liu L. Linear depolarization of lidar returns by aged smoke
544     particles. Appl Opt. 55, 9968-9973, doi: 10.1364/AO.55.009968, 2016.

545 Ohneiser, K., Ansmann, A., Baars, H., Seifert, P., Barja, B., Jimenez, C., Radenz, M., Teisseire,
546     A., Floutsi, A., Haarig, M., Foth, A., Chudnovsky, A., Engelmann, R., Zamorano, F., Bühl,

J., and Wandinger, U.: Smoke of extreme Australian bushfires observed in the stratosphere over Punta Arenas, Chile, in January 2020: optical thickness, lidar ratios, and depolarization ratios at 355 and 532 nm, Atmos. Chem. Phys., 20, 8003–8015, https://doi.org/10.5194/acp-20-8003-2020, 2020.

Peterson, D.A., Campbell, J.R., Hyer, E.J. et al. Wildfire-driven thunderstorms cause a volcano-like stratospheric injection of smoke, npj Clim. Atmos. Sci. 1, 30, 2018. https://doi.org/10.1038/s41612-018-0039-3

Rao, Z., He, T., Hua D, Wang, Y., Wang, X., Chen, Y., Le J.: Preliminary measurements of fluorescent aerosol number concentrations using a laser-induced fluorescence lidar, Appl. Opt. 57, 7211-7215, https://doi.org/10.1364/AO.57.007211, 2018.

Reichardt, J.: Cloud and aerosol spectroscopy with Raman lidar, J. Atmos. Ocean. Tech., 31, 1946–1963, https://doi.org/10.1175/JTECH-D-13-00188.1, 2014.

Reichardt, J., Leinweber, R., Schwebe, A.: Fluorescing aerosols and clouds: investigations of co-existence, EPJ Web Conf., 176, 05010, https://doi.org/10.1051/epjconf/201817605010, 2018.

Reichardt, J., Behrendt, O., and Lauermann, F.: Spectrometric fluorescence and Raman lidar: absolute calibration of aerosol fluorescence spectra and fluorescence correction of humidity measurements, Atmos. Meas. Tech., 16, 1–13, 2023. https://doi.org/10.5194/amt-16-1-2023.

Richardson, S.C., Mytilinaios, M., Foskinis, R., Kyrou, C., Papayannis, A., Pyrri, I., Giannoutsou, E., Adamakis, I.D.S.: Bioaerosol detection over Athens, Greece using the laser induced fluorescence technique, Science of the Total Environment 696, 133906, 2019. https://doi.org/10.1016/j.scitotenv.2019.133906

Sugimoto, N., Huang, Z., Nishizawa, T., Matsui, I, Tatarov, B.: Fluorescence from atmospheric aerosols observed with a multichannel lidar spectrometer," Opt. Expr. 20, 20800-20807, https://doi.org/10.1364/OE.20.020800, 2012.

Veselovskii, I., Whiteman, D. N., Korenskiy, M., Suvorina, A., and Pérez-Ramírez, D.: Use of rotational Raman measurements in multiwavelength aerosol lidar for evaluation of particle backscattering and extinction, Atmos. Meas. Tech., 8, 4111–4122, https://doi.org/10.5194/amt-8-4111-2015, 2015.

Veselovskii, I., Hu, Q., Goloub, P., Podvin, T., Korenskiy, M., Pujol, O., Dubovik, O., Lopatin, A.: Combined use of Mie-Raman and fluorescence lidar observations for improving aerosol

577  characterization: feasibility experiment, Atm. Meas. Tech., 13, 6691–6701, 2020.
578      doi.org/10.5194/amt-13-6691-2020.

579  Veselovskii, I., Hu, Q., Goloub, P., Podvin, T., Barchunov, B., and Korenskii, M.: Combining
580      Mie–Raman and fluorescence observations: a step forward in aerosol classification with lidar
581      technology, Atmos. Meas. Tech., 15, 4881–4900, 2022. https://doi.org/10.5194/amt-15-4881-
582      2022.

583  Veselovskii, I., Kasianik, N., Korenskii, M., Hu, Q., Goloub, P., Podvin, T., and Liu, D.:
584      Multiwavelength fluorescence lidar observations of smoke plumes, Atmos. Meas. Tech., 16,
585      2055–2065, 2023. https://doi.org/10.5194/amt-16-2055-2023

586  Whiteman, D. N.: Examination of the traditional Raman lidar technique. I. Evaluating the
587      temperature    dependent    lidar    equations,    Appl.    Optics,    42,    2571–2592,
588      https://doi.org/10.1364/AO.42.002571, 2003.

589

590
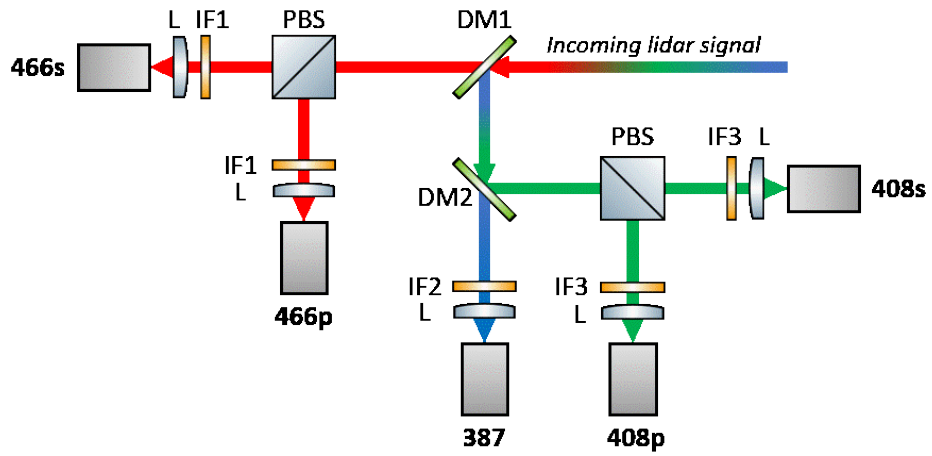
591

592    Fig.1. Optical layout of depolarization measurements at 408 nm and 466 nm wavelengths. L –
593    lens; IF1- IF3 – interference filters, DM1, DM2 – dichroic mirrors, PBS – polarizing cube.

594

595

596

597
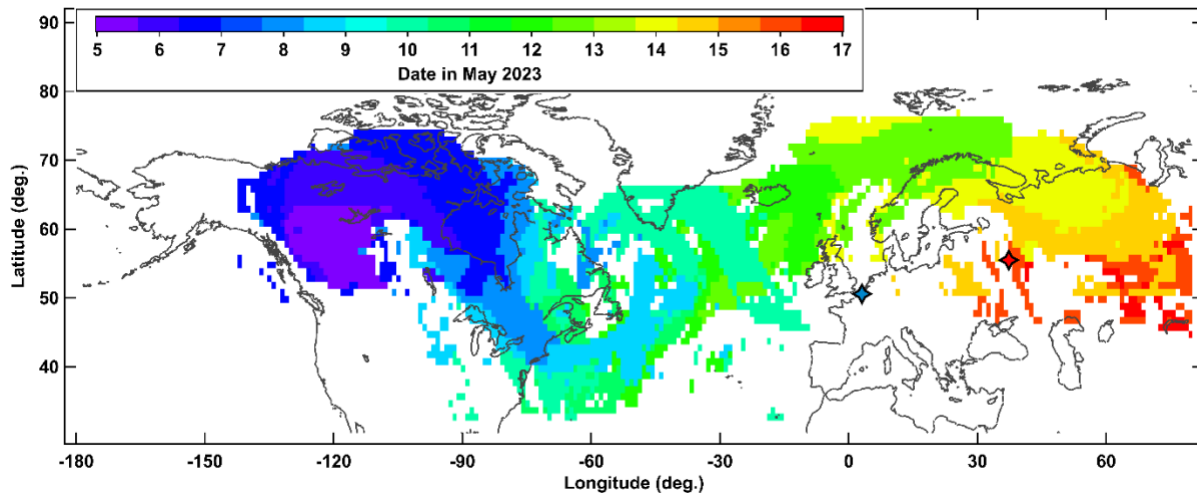
Fig.2. Spatio-temporal evolution of the smoke plume from the wildfire event in Alberta, Canada on 5 May 2023. Color-filled time-coded areas indicate the Aerosol Index (AI) values from the OMPS-NPP instrument exceeding 0.5. The blue and red-filled stars indicate the location of Lille and Moscow lidar stations, respectively.

602

603
604
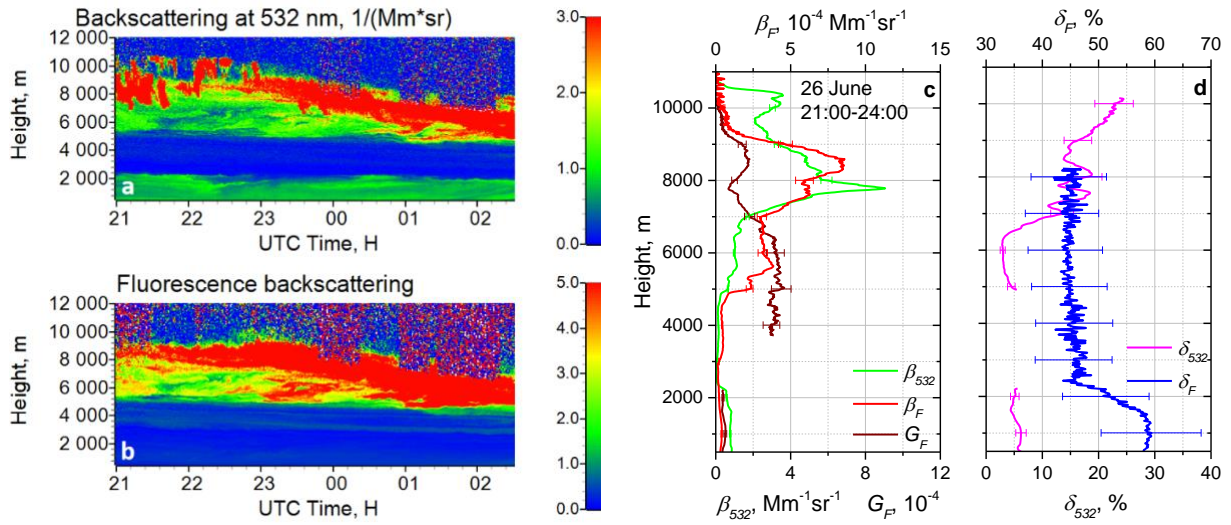
605
606 Fig.3. Smoke event on the night 26-27 June 2023 over Lille. Spatio-temporal distributions of (a)
607 aerosol backscattering coefficient $\beta_{532}$ and (b) fluorescence backscattering $\beta_F$ (in $10^{-4}$ $Mm^{-1}sr^{-1}$).
608 Vertical profiles of (c) the aerosol $\beta_{532}$ and fluorescence $\beta_F$ backscattering coefficients, the
609 fluorescence capacity $G_F$; (d) the particle $\delta_{532}$ and the fluorescence $\delta_F$ depolarization ratios.
610
611
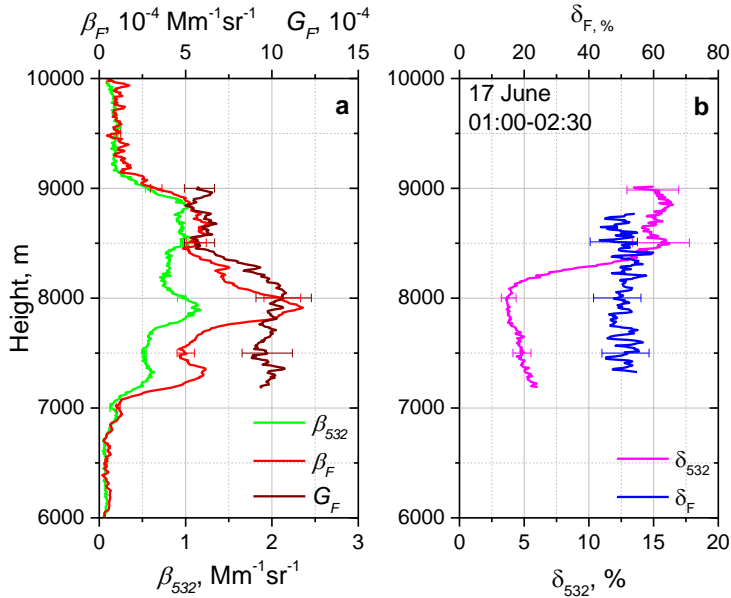
612
613 Fig.4. Vertical profiles of (a) aerosol $\beta_{532}$ and fluorescence $\beta_F$ backscattering coefficients,
614 fluorescence capacity $G_F$ and (b) particle $\delta_{532}$ and fluorescence $\delta_F$ depolarization ratios on the night
615 16-17 June 2023 for period 01:00-02:30 UTC over Lille.
616
617

618
619
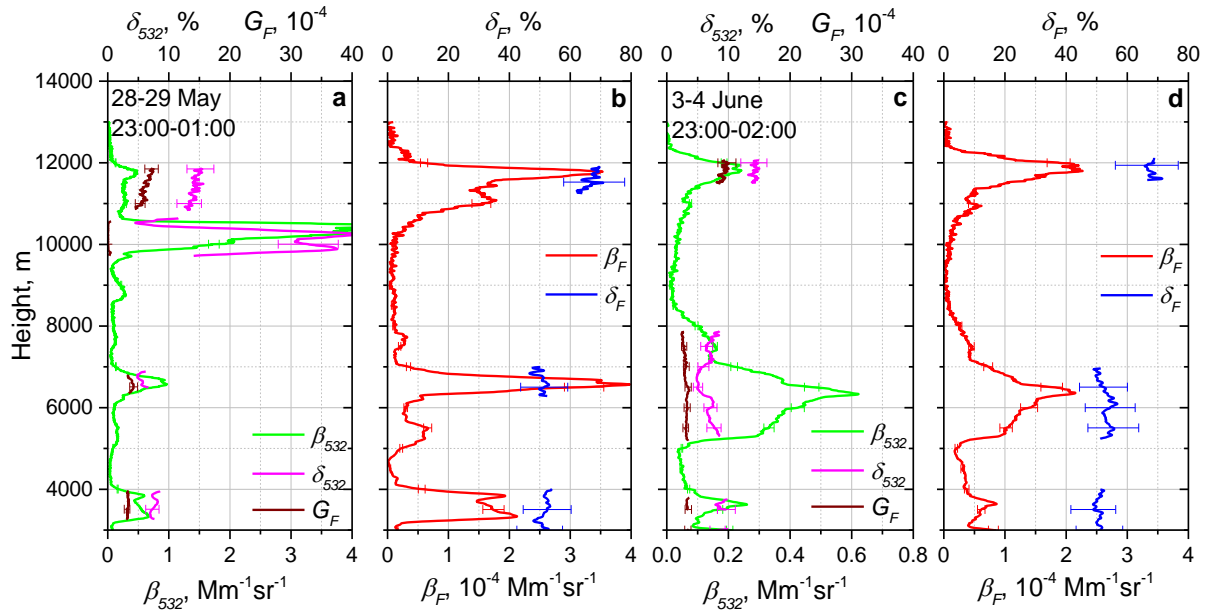
620
621 Fig.5. Vertical profiles of (a, c) backscattering coefficient $\beta_{532}$, particle depolarization ratio $\delta_{532}$,
622 fluorescence capacity $G_F$ and (b, d) fluorescence backscattering $\beta_F$ and fluorescence depolarization
623 ratio $\delta_F$ for two smoke episodes on the nights 28-29 May 2023 and 3-4 June 2023 over Lille.
624
625

626

627
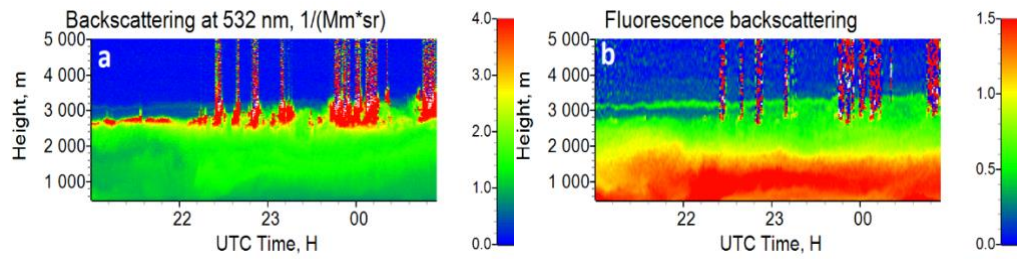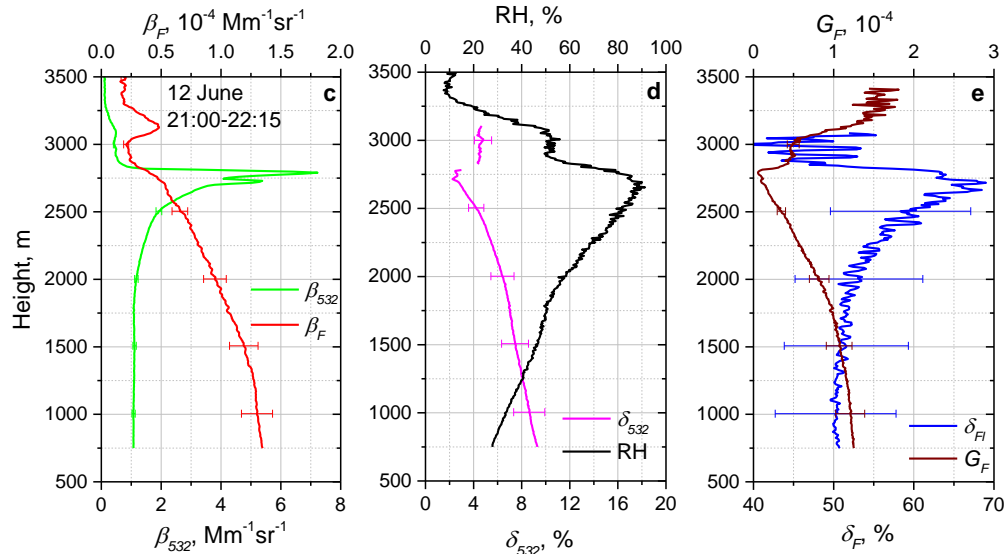
628
629 Fig.6. Particle hygroscopic growth in the PBL on the night 12-13 June 2023 over Lille. Spatio-
630 temporal distributions of (a) aerosol backscattering coefficient $\beta_{532}$ and (b) fluorescence
631 backscattering $\beta_F$ (in $10^{-4}$ $Mm^{-1}sr^{-1}$). Vertical profiles of (c) aerosol $\beta_{532}$ and fluorescence $\beta_F$
632 backscattering coefficients; (d) particle depolarization ratio $\delta_{532}$ and the relative humidity RH; (e)
633 fluorescence depolarization ratio $\delta_F$ and fluorescence capacity $G_F$ for the time period 21:00-22:15
634 UTC.
635

636
637
638
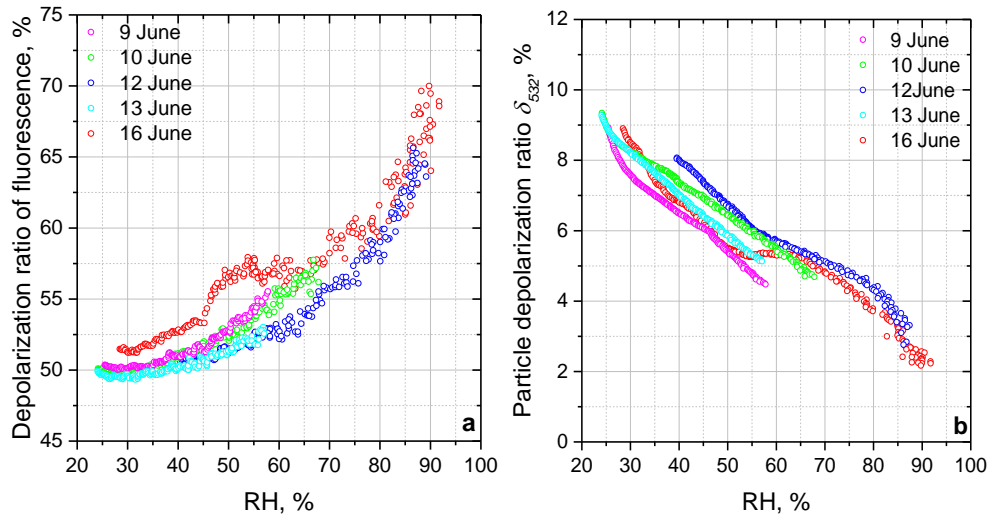
639
640 Fig.7. (a) Fluorescence depolarization ratio and (b) particle depolarization ratio $\delta_{532}$ as a function
641 of the relative humidity in the PBL for the measurements on 9, 10, 12, 13, 16 June 2023 over Lille.
642
643

644
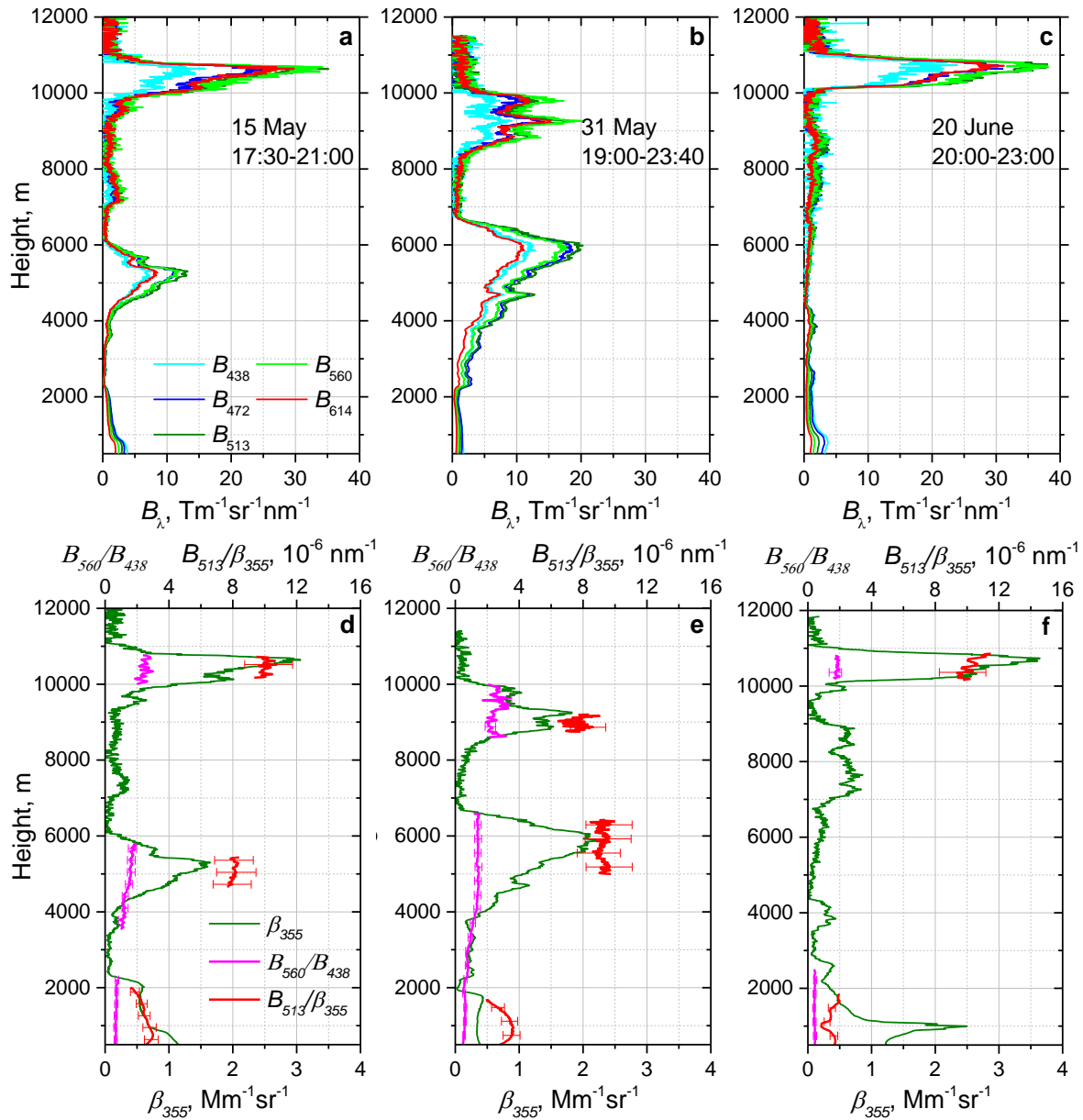
645
646 Fig. 8. Fluorescence measurements over Moscow on 15 May, 31 May, 20 June 2023. Vertical
647 profiles of (a-c) fluorescence spectral backscattering coefficients $B_\lambda$ at 438, 472, 513, 560, 614 nm
648 and (d-f) aerosol backscattering coefficient $\beta_{355}$, the ratio $B_{560}/B_{438}$ and $B_{513}/\beta_{355}$. Measurements
649 were performed at an angle of $48^0$ to horizon.
650
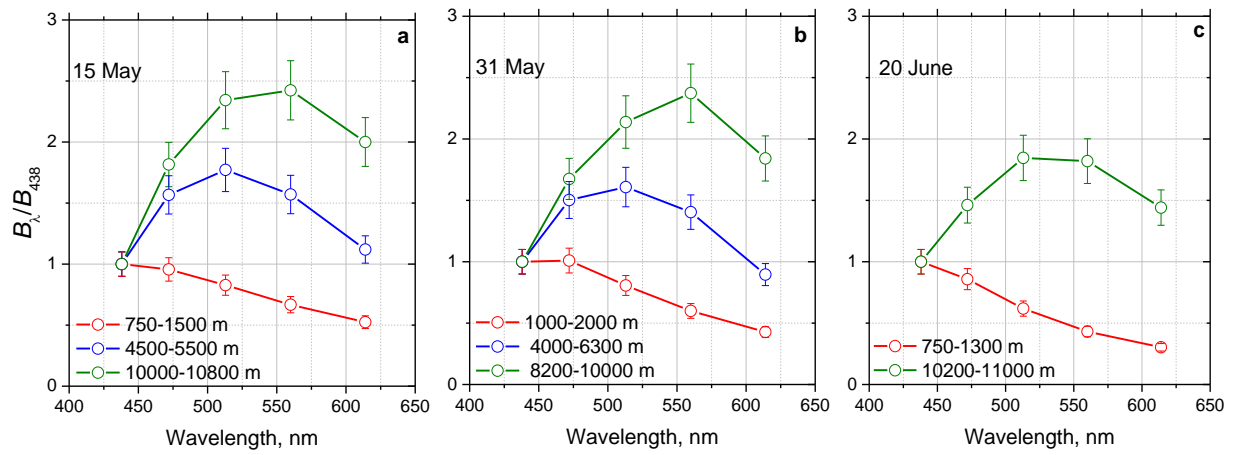
651

652 Fig.9. Fluorescence spectra $B_\lambda/B_{438}$ at different height intervals measured during smoke episodes
653 on 15 May, 31 May, 20 June 2023 over Moscow, for the same temporal intervals as in Fig.8.
654
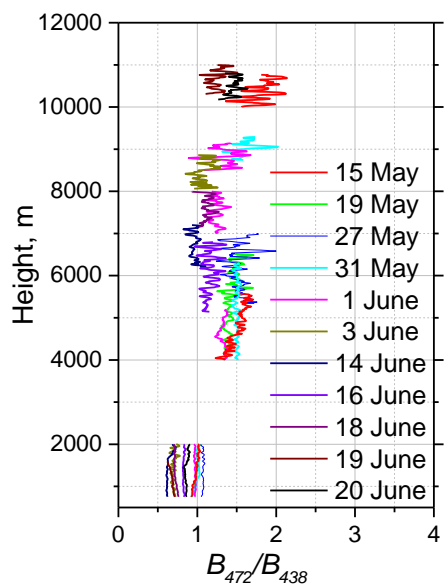
655

656 Fig.10. Height profiles of the ratio $B_{472}/B_{438}$ for smoke episodes during 15 May – 20 June 2023
657 over Moscow. Smoke layers start above 4 km up to 11 km.

658

659

660
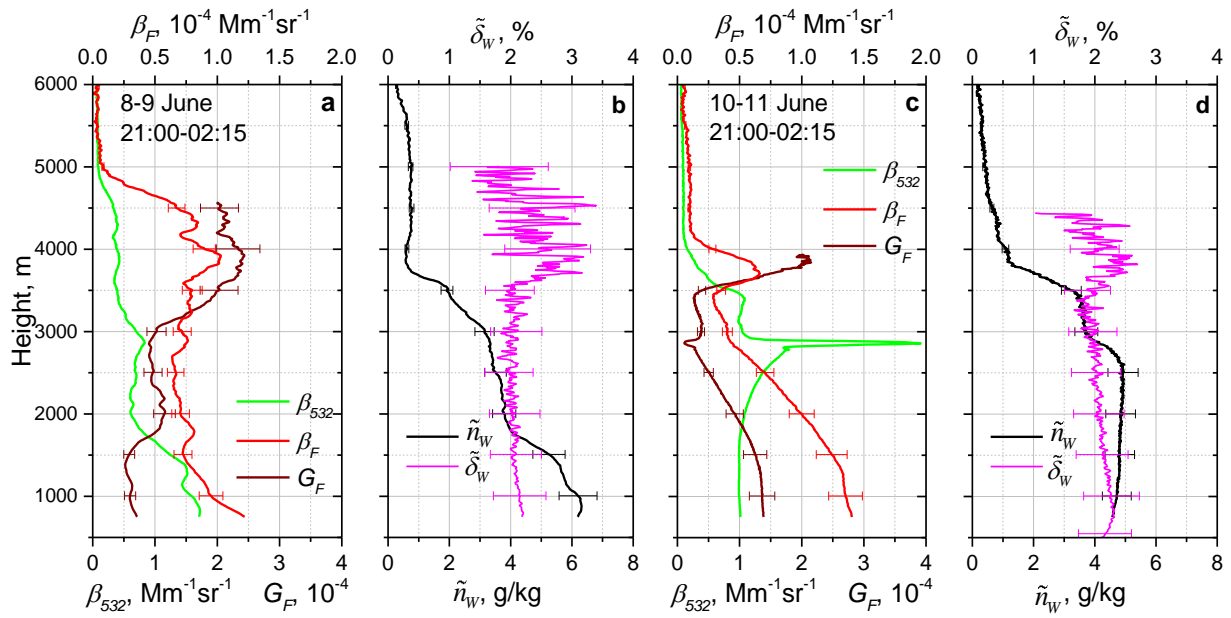
661 Fig.11. Impact of the aerosol fluorescence on the depolarization ratio in the water vapor Raman
662 channel on the nights 8-9 and 10-11 June 2023 over Lille. Vertical profiles of (a, c) particle
663 backscattering $\beta_{532}$, fluorescence backscattering $\beta_F$, fluorescence capacity $G_F$ and (b, d)
664 depolarization ratio $\tilde{\delta}_W$ of the water vapor Raman signal and the water vapor mixing ratio $\tilde{n}_W$ .

665
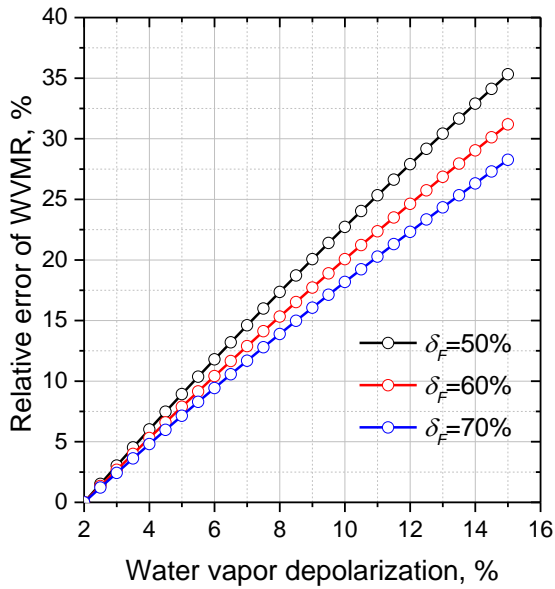
666

667    Fig.12. Relative error of water vapor mixing ratio (WVMR) $\frac{\Delta n_W}{\tilde{n}_W}$ induced by the fluorescence as

668    a function of depolarization ratio $\tilde{\delta}_W$ in the water vapor Raman channel for three values of

669    fluorescence depolarization ratio $\delta_F$=50%, 60%, 70%. The depolarization ratio of water vapor

670    Raman backscatter in the absence of fluorescence is assumed to be $\delta_W$=2%.

671

672

673
674
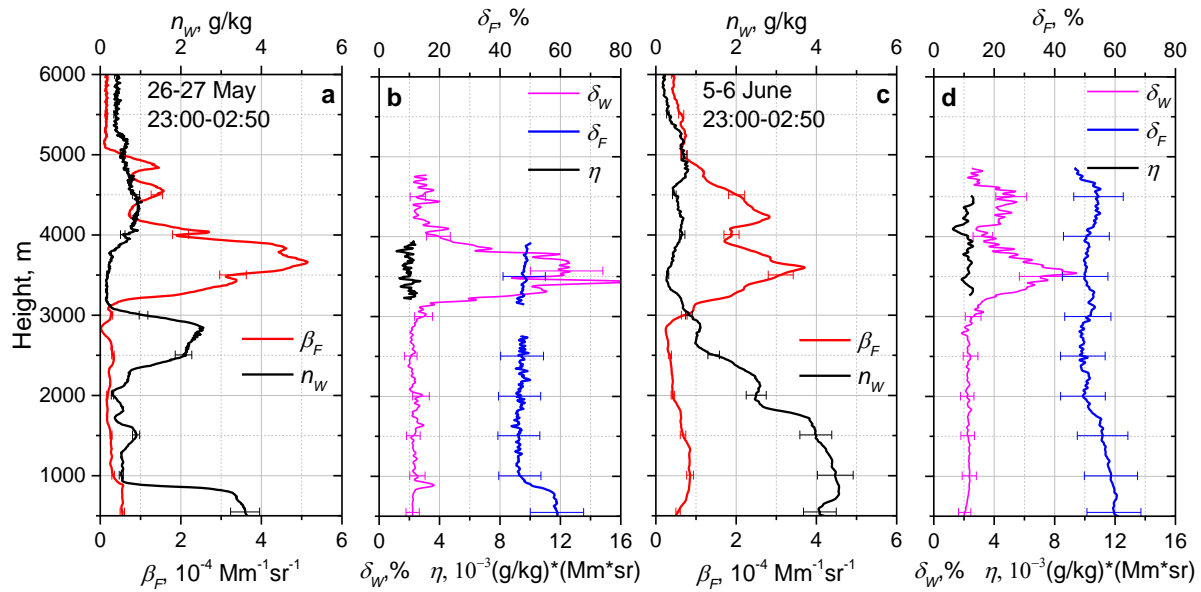
675

676 Fig. 13. Fluorescence measurements over Lille on the night 26-27 May and 5-6 June 2023. (a, c)
677 Vertical profiles of the fluorescence backscattering $\beta_F$, the water vapor mixing ratio $\tilde{n}_W$, (b, d) the
678 depolarization ratio of the water vapor Raman signal $\tilde{\delta}_W$, the fluorescence depolarization ratio $\delta_F$
679 and parameter $\eta$, describing contribution of the fluorescence to the water vapor channel.
680

681

682
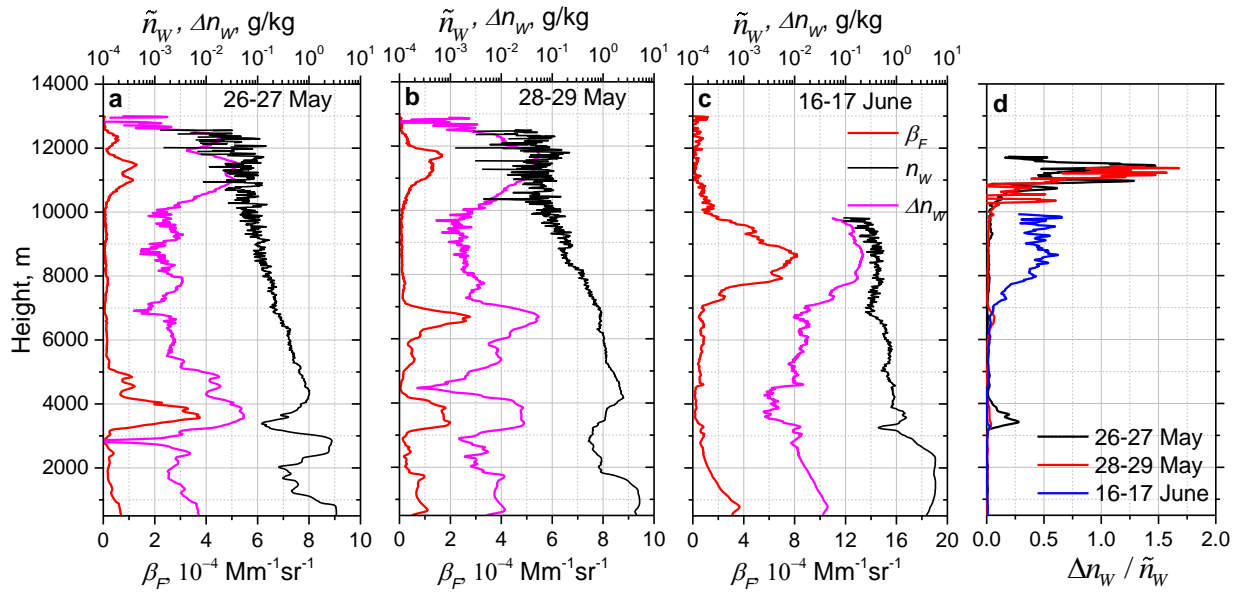
683
684 Fig.14. Impact of smoke fluorescence on the water vapor measurements. Vertical profiles of the
685 fluorescence backscattering $\beta_F$, water vapor mixing ratio $\tilde{n}_W$ and bias in water vapor channel $\Delta n_W$
686 provided by the fluorescence of smoke for episodes on the nights (a) 26-27 May, (b) 28-29 May
687 and (c) 16-17 June 2023 for time interval 21:00-02:30 UTC over Lille. (d) Error $\dfrac{\Delta n_W}{\tilde{n}_W}$ introduced
688 by smoke fluorescence for the three episodes.
689